

Plot level rapid screening for photosynthetic parameters using proximal hyperspectral imaging

Katherine Meacham-Hensold^{1,2}, Peng Fu², Jin Wu^{3,4}, Shawn Serbin³, Christopher M. Montes¹, Elizabeth Ainsworth^{5,1,2}, Kaiyu Guan^{6,7}, Evan Dracup⁵, Taylor Pederson², Steven Driever^{2,8} and Carl Bernacchi^{*5,1,2}.

¹Department of Plant Biology, University of Illinois at Urbana-Champaign.

²Carl R Woese Institute for Genomic Biology, University of Illinois at Urbana-Champaign.

³Environmental & Climate Science Department, Brookhaven National Laboratory, Upton, New York, USA.

⁴School of Biological Sciences, University of Hong Kong, Pokfulam, Hong Kong.

⁵USDA ARS Global Change and Photosynthesis Research Unit, Urbana, IL, USA.

⁶Department of Natural Resources and Environmental Sciences, University of Illinois at Urbana-Champaign, IL, USA.

⁷National Center of Supercomputing Applications, University of Illinois at Urbana-Champaign, USA.

⁸Center for Crop Systems Analysis, Wageningen University, Netherlands.

Highlight

We present a plot-level tool to predict photosynthetic parameters and pigment contents with PLSR analysis of sunlit leaf reflectance pixels to offer high throughput field screening for improved photosynthetic performance.

Abstract

Photosynthesis is currently measured using time laborious and/or destructive methods which slows research and breeding efforts to identify crop germplasm with higher photosynthetic capacities. We present a plot level screening tool for quantification of photosynthetic parameters and pigment contents that utilizes hyperspectral reflectance from sunlit leaf pixels collected from a plot (~2mx2m) in less than one minute. Using field grown *Nicotiana tabacum* with genetically altered photosynthetic pathways over two growing seasons (2017 and 2018), we built predictive models for eight photosynthetic parameters and pigment traits. Using partial least squares regression (PLSR) analysis of plot-level sunlit vegetative reflectance pixels from a single VNIR (400-900nm) hyperspectral camera, we predict maximum carboxylation rate of Rubisco ($V_{c,max}$, $R^2=0.79$) maximum electron transport rate in given conditions (J_{1800} , $R^2=0.59$), maximal light saturated photosynthesis (P_{max} , $R^2=0.54$), chlorophyll content (Chl , $R^2=0.87$), the ratio of chlorophyll a to b ($Chl\ a:b$, $R^2=0.63$), carbon content (C, $R^2=0.47$) and nitrogen content (N, $R^2=0.49$). Model predictions did not improve when using two cameras spanning 400-1800nm suggesting a robust, widely applicable and more ‘cost-effective’ pipeline requiring only a single VNIR camera. The analysis pipeline and methods can be used in any cropping system with modified species specific PLSR analysis to offer a high throughput field phenotyping screening for germplasm with improved photosynthetic performance in field trials.

Key words

Hyperspectral imaging, photosynthesis, spectral reflectance, food security, proximal sensing, field phenotyping.

Abbreviations

C – Carbon content (%)

EVI – enhanced vegetation index

GPP – gross primary productivity

J_{1800} – maximum electron transport rate at 1800 $\mu\text{mol m}^{-2} \text{s}^{-1}$ PAR

J_{max} - maximum electron transport rate

N – Nitrogen content (%)

55 NDVI – normalized difference vegetation index
 56 NIR - near infra-red electromagnetic energy
 57 ϕCO_2 – quantum yield of carbon fixation
 58 PLSR – partial least squares regression
 59 P_{max} - maximum light saturated photosynthetic rate
 60 SIF – solar induced fluorescence
 61 SWIR - shortwave infra-red electromagnetic energy
 62 $V_{c,max}$ – maximum carboxylation rate of Rubisco
 63 VIP – variable importance projection
 64 VIS – visible electromagnetic energy
 65 VNIR - visible near infra-red electromagnetic energy
 66

67 **Introduction**

68 Projected population increase and pressures on land and agricultural resource availability
 69 induced by a changing global climate is placing increased demand to secure global food supply
 70 in coming decades (Foley et al., 2011; Tilman et al., 2009). Improving photosynthetic capacity
 71 has become a target to enable crop yield increase (Evans, 2013; Zhu et al., 2010; Long et al.,
 72 2006; Monteith and Moss, 1977). Inefficiencies in the photosynthetic pathway have inspired
 73 research efforts to exploit natural variation in photosynthetic capacity (Lawson et al., 2012), and
 74 to improve photosynthetic pathways transgenically (Ort et al., 2015). Thus, crop scientists and
 75 breeders face the challenge of characterizing genetic improvements in field trials in a high
 76 throughput manner as a screening tool to identify ‘photosynthetically superior’ germplasm
 77 (Furbank and Tester, 2011). While photosynthetic capacity has been successfully estimated from
 78 hyperspectral imaging at the ecosystem scale (Serbin et al., 2015) it is often too coarse in spatial
 79 resolution to discriminate in mixed germplasm field trials. Where hyperspectral analysis has
 80 predicted leaf-level photosynthetic capacities and pigment contents (Ainsworth et al., 2014;
 81 Serbin et al., 2012; Silva-Perez et al., 2017; Yendrek et al., 2016) it holds limitation as leaf clip
 82 measurements only pinpoint a few individual leaves in a plot canopy. Currently there are limited
 83 tools to screen a whole plot, rather than individual leaves, for photosynthetic performance. Plot
 84 level estimations with proximal sensing platforms are needed to allow rapid capture of

reflectance from all sunlit vegetation in sensor range, eliminating the need to make assumptions about plot performance based on leaf-level samples, and expanding the spatial and temporal capabilities of analysis to capture hundreds of plots in a single day.

The maximum carboxylation rate of Rubisco ($V_{c,max}$) and maximum electron transport rate in given conditions (J_{max}) are widely used as determinants of photosynthetic capacity for the carbon reduction cycle and the electron transport chain respectively (Caemmerer and Farquhar, 1981; von Caemmerer, 2000) and are traditionally derived at the leaf level with infra-red gas exchange analysis. The response of leaf-level CO_2 assimilation to incrementing CO_2 is measured (Long and Bernacchi, 2003) and analyzed (Sharkey et al, 2007) according to the mechanistic model of photosynthesis (Farquhar et al. 1980). The quantum yield of CO_2 fixation (ϕCO_2) and maximum light saturated photosynthetic rates (P_{max}) are also used as determinants of photosynthetic operating efficiency, as derived from leaf-level gas exchange measurements of the response of CO_2 assimilation to incrementing photosynthetically active radiance (PAR) (Ögren and Evans, 1993). Due to the wealth of physiological information provided, leaf level gas exchange has dominated retrieval of these photosynthetic parameters for decades, but it is limited and time restrictive for the sampling required to measure large crop trials. Additionally, upscaling from leaf gas exchange to determine plot or canopy photosynthetic capacity from gas exchange often requires complex modeling with many assumptions (De Pury and Farquhar, 1997; de Wit, 1965; Evans and Farquhar, 1991; Wu et al., 2019; Yin and Struik, 2017).

Recently, advances have been made in quantifying photosynthesis from spectral analysis at the leaf to ecosystem scales. At the leaf level, with a hand held spectral leaf gun photosynthetic capacity ($V_{c,max}$ and J_{max}) and Chlorophyll (Chl), Carbon (C) and Nitrogen (N) content have been predicted successfully from hand-held reflectance spectroscopy across the full electromagnetic spectrum (400-2500nm) for tree species (Serbin et al., 2012; Serbin et al., 2014), productive cropping systems (Ainsworth et al., 2014; Ely et al., 2019; Silva-Perez et al., 2017; Yendrek et al., 2016), and in field trials of *N. tabacum* with altered photosynthetic pathways (Fu et al., 2019; Meacham-Hensold et al., 2019). Partial least squares regression (PLSR) analysis of reflectance spectra has also been applied to predict photosynthetic capacity with airborne hyperspectral imaging at the agroecosystem canopy scale (Serbin et al., 2015), however, the most advanced systems satellite hyperpspectral systems capture around 1 pixel per 10-30m

(Transon et al. 2018), which is too coarse in spatial resolution to identify genotypic variation within field trials of many small plots. Advanced UAV systems are able to capture greater spatial resolution (~40cm per pixel) (Ruwaimana et al., 2018, Zarco-Tejada et al., 2013) but still fall short of the millimeter resolution required to build models to predict photosynthetic capacities at the scale of individual leaves in small plots. While multispectral cameras are widely available at higher resolution and used to derive plot level spectral vegetation indices (SVI's) from discrete spectral wavelengths (Curran et al., 1990; Gamon et al., 1992; Haboudane et al., 2004; Thenkabail et al., 2000; Zarco-Tejada et al., 2002), SVI's are not able to determine photosynthetic parameters beyond structural inference on physiological processes from discrete spectral bands. Satellite mounted multi-spectral imaging systems have also been widely exploited to derive spectral indices such as the enhanced vegetation index (EVI) and normalized difference vegetation index (NDVI), and more recently solar-induced fluorescence (SIF) (Guan et al., 2016; Guanter et al., 2014; Porcar-Castell et al., 2014) and linked to ecosystem gross primary productivity (GPP) (Barnes et al., 2017; He et al., 2019; Rahman et al., 2005; Shi et al., 2017; Smith et al., 2002; Wylie et al., 2003; Zhang et al., 2014; Zhang et al., 2018). Multi spectral SVI and SIF estimates have been incorporated into terrestrial biosphere models to predict photosynthetic capacities at the ecosystem scale (Demarty et al., 2007; Kattge et al., 2009; Zhang et al., 2014), but have not been used to predict photosynthetic capacity in smaller scale plot trials.

Resolving hyperspectral analysis of photosynthetic parameters at the plot level holds many practical and technical challenges. First, hyperspectral cameras and sensors that capture reflectance at the spatial and spectral resolution required for plot level analysis are often limiting in terms of availability, affordability and suitability for field trial scanning. Second, field phenotyping proximal sensing platforms (Deery et al., 2014) to house such sensors are not currently commercially available and need to be fabricated for purpose. Third, hyperspectral imaging systems generate memory intensive three dimensional datasets with two spatial dimensions (S_x and S_y) and one spectral (S_λ) forming 'hypercubes' (Bannon, 2009), necessitating advanced data storage systems and custom analysis pipelines. Fourth, at the plot level, plant geometrical structure, leaf scattering properties, background soil and dynamic environmental conditions (Gao et al., 2000; Jay et al., 2016; Verhoef, 1984; Vogelmann et al., 1996) need to be resolved against leaf-level 'ground truth' measurements to accurately infer photosynthetic

performance upscaled from leaf to plot level. And finally, ensuring use of this technology relates to important physiological questions requires effective interdisciplinary collaboration between engineering, computational and biological specialists.

In this study, we present a plot level high throughput phenotyping platform housing two hyperspectral cameras. One VNIR camera captured reflectance from 400-900nm spectral resolution 2.1nm and the second NIR/SWIR camera from 900-1800nm (spectral resolution 4.9nm). We created an automated hyperspectral imaging processing pipeline that extracts plot level sunlit vegetation pixel reflectance spectrum to predict $V_{c,max}$, J_{1800} , Chl , $Chl\ a:b$, C , N , P_{max} and ϕCO_2 . From partial least squares regression (PLSR) analysis of plot-level reflectance spectra from hyperspectral images, we predict these photosynthetic traits in field trials of wild-type and genetically modified lines of *N. tabacum*. We assess the contribution of spectral regions and the applicability of this technique to the field phenotyping community and offer a tool for high throughput phenotyping of large-scale crop trials to facilitate screening for increasing crop yields.

Methods

Data from two growing seasons (2017 and 2018) were used in this study, presented in two performance tests. For performance test 1, three wild type and seven transgenic *N. tabacum* lines were measured over 2017 and 2018 growing seasons (Table 1). Measurements in 2017 were taken from June 22nd – August 1st and in 2018 on July 24th and 25th. For performance test 2, two wild type and eight transgenic *N. tabacum* were measured in 2018 on July 26, 27 and 28th. In performance test 1, predictive models were built from hyperspectral reflectance (both leaf and plot-level) with ground truth data from gas exchange measurement of CO_2 response curves for $V_{c,max}$ and J_{1800} , and leaf pigment extractions for chlorophyll content (Chl), chlorophyll a:b ($Chl\ a:b$), Carbon content (C) and Nitrogen content (N). For performance test 2, predictive models for plot and leaf-level P_{max} and ϕCO_2 were trained with ground truth data from gas exchange measurement of light response curves.

Plant material

In 2017, three wild type *N. tabacum* cultivars and six transgenically modified lines (described in detail in Table 1) were grown at the University of Illinois Energy Farm Facility in Urbana, Illinois (40°03'46.4"N 88°12'25.4"W, 215 m above sea level). All experiments consisted of four replicated plots of each genotype arranged in a 6 × 6 grid and spaced 0.38 m apart with 36 plants per plot. Each plot measured approx. 2x2 meters. All transgenic material is expressed in the Petite Havana background, with the exception of the Rubisco antisense lines in the W38 background. Seedlings were germinated in greenhouse conditions in float trays using a coir soil mix (Coco loco) maintained daily at 150ppm N using a 20-20-20 general purpose water soluble fertilizer. Plants were and transplanted to the field at the four-leaf stage. High levels of ESN Smart Nitrogen (310 kg/ha, ~150ppm soil concentration) were applied to the field site two weeks prior to transplanting. A broad action herbicide, Glyphosate-isopropylammonium (41%) (Killzall; VPG) (15 l at 70g/l) was applied once to all plots two days prior to transplanting. A biological pesticide *Bacillus thuringiensis v. kurstaki* (54%) (DiPel PRO), was applied to the prepared field site five days prior to transplant and at biweekly intervals thereafter to control for tobacco pests. Irrigation was provided to all plots as needed to eliminate water limitation throughout growth.

In 2018, two wild type, four previously grown transgenic lines, and four newly added transgenic lines (described in detail in Table 1) were grown according to the same protocol as 2017. All transgenic plant material was homozygous with the exception of single Rubisco antisense and decreased PsbS line (4-KO). Single Rubisco antisense plants were planted to the field without screening. 4-KO seedlings were screened 8 days post emergence with chlorophyll fluorescence imaging to identify and select only plants with the PsbS knockout phenotype for low non-photochemical quenching (NPQ).

Hyperspectral image collection

A ground-based field phenotyping platform was built to house two hyperspectral push-broom cameras mounted on a horizontal beam (Fig 1A). The first hyperspectral imaging camera (PIKA II: Resonon, Inc., Bozeman, MT, USA) captured spectral radiation from 400 to 900 nm in 2.1 nm contiguous bands (240 spectral bands total) with 640 spatial channels. The second camera (PIKA NIR: Resonon, Inc.) recorded spectral radiation from 900 to 1800 nm in 4.9 nm contiguous bands (164 spectral bands) with 320 spatial channels. Both cameras were mounted at

a height of 1.6 m from soil and were triggered simultaneously above a plot to acquire two images during a ~30s scan. Images were captured in high irradiance conditions during a 3hr window around solar noon and stored using SpectronPro software (*Resonon, Inc.*). A 99% reflective white Teflon panel was mounted horizontally and level with the top of the plant canopy and captured in the field of view for each image (Fig. 1B). Images were captured and stored in raw data mode. The cameras were calibrated to remove electrical and dark current daily prior to data acquisition. Camera integration time was set at 20% below saturation point according to the radiance signal from the Teflon panel before each scan to avoid saturation.

Hyperspectral image analysis pipeline

An automated image analysis pipeline was created using Python (*Python Software Foundation, <https://www.python.org/>*), to extract spectral reflectance from images acquired in raw data mode (Fig 2B). Data from each camera went through the same three phases of processing: first, conversion of raw data in digital numbers to radiance using radiometric calibration, second, the classification of pixels (Fig. 2B) and third, conversion of radiance pixels to reflectance (Fig 2C). For the first phase, raw data were converted to absolute radiance using radiometric calibration files from the camera manufacturer. In the second phase, the image was segregated to represent 6 matter classifications using K-means clustering (Spath, 1985) which separated pixels of interest (sunlit leaves and Teflon) from shaded leaves, soil, platform shadow, and non-biological matter. Thirdly, reflectance (R) was calculated using the radiance signature from the Teflon white reference captured in each image against a lab calibrated Teflon standard using equation 1:

$$R = \frac{S_{sunlit}}{S_{ref}} * R_{ref} \quad (1)$$

where S_{sunlit} is radiance from sunlit leaves, S_{ref} is radiance from the Teflon panel, and R_{ref} is the percentage reflectance from lab calibrated Teflon standard. Reflectance from all sunlit pixels in each image was averaged per plot (Fig 2D). Spectral reflectance from both cameras in the same plot was joined to give reflectance for sunlit leaves per plot from 400-1800nm. Spectra were filtered with a polynomial order of 2 using 11 spectral measurements (nm) as the window length (Savitzky and Golay, 1964). Prior to PLSR analysis spectral bands below 450nm and above

1700nm were removed due to excess noise, and between 1313 and 1440nm were removed due to atmospheric water absorption (Hill and Jones, 2000; Serbin et al., 2015).

Leaf spectral measurements

Leaf-level spectral measurements were made using a spectroradiometer (Fieldspec4, Analytical Spectral Devices - ASD, Boulder, CO USA), with a leaf clip attached to a fiber optic cable. Leaf spectral reflectance was measured *in situ* from 400-2500nm with spectral resolution of 3nm in the visible and NIR (350-1000nm) and 8nm in shortwave-infrared (SWIR; 1000-2500nm). The device houses a radiometrically calibrated light source which was standardized for relative reflectance prior to measurement using a Spectralon (Labsphere Inc., North Dutton, NH, USA) panel for white reference. In 2017 three leaves were sampled per plot and five per plot in 2018. Measurements were made on the last fully expanded leaf, maintaining natural leaf orientation avoiding leaf midrib and edges. On a single leaf, six reflectance spectra were recorded using the leaf clip attachment in different regions of the same leaf. The six spectra for a single leaf were then averaged to give a mean spectrum per leaf. Each single measurement was the mean of 10 scans at a scan speed of 100ms. A spectral splice correction was applied to each spectrum to remove heat drift effects that may shift the sensors and align the VIS and SWIR to the NIR sensors within the Fieldspec4, using the FieldSpectra package in R according to Serbin et al. (2014). For quality control, spectra with abnormally high light levels at 450nm were excluded from analysis to ensure the leaf clip was properly fastened onto the leaf for each measurement. Spectral samples with a deviation from the mean reflectance greater than 2% were eliminated from analysis along with leaves with less than 4 viable spectra.

Predictive PLSR models for all traits were built at both leaf and canopy levels for comparisons. For plot level models, the averaged ground truth subsamples (three leaf measurements in 2017 and five leaf measurements in 2018) from each plot were used as input for model build and validation. For leaf-level models, each individual leaf subsample measurement was included as a training data point without averaging per plot.

PLSR analysis

Predictive models were built for 8 traits, following PLS principles (Wold et al., 2001) according to the protocol of Serbin et al. (2014), modified for *N. tabacum*. Although in our

previous work (Fu et al., 2019) multiple stacked machine learning algorithms showed increased predictability (+5% for R^2) of photosynthetic capacity ($V_{c,max}$), we used PLSR only in this work given the ability to derive scaling coefficients across the electromagnetic spectra from this technique, which allow inference of important contributing regions of the spectra for trait prediction. Unlike other predictive algorithms, PLSR coefficient loadings can be calculated to infer the physiological importance of specific spectral bands based on known vegetation spectral properties, and thus can be used to confirm the biological relevance of model builds between different devices and scales.

We used the open-source PLS package (Mevik and Wehrens 2007) in R (*The R Foundation for Statistical Computing, Wien, Austria*) to create a linear model of waveband coefficients that account for trait variation in reflectance spectra. The optimal number of components (latent variables: LV's) for each model build was determined from the minimum root mean square error (RMSE) of the predicted residual sum of squares (PRESS) statistic (Esbensen et al., 2002), using a leave-one-out cross validation approach that then makes a prediction for the out-of-sample observation (Siegmann and Jarmer, 2015). This prevents overfitting. Models were trained with data pairs of leaf or plot reflectance and a ground truth measurement, and cross validated with 1000 times random resampling to determine model stability. All model R^2 presented herein are from this cross validation (CV). Loading weights indicate known spectral peaks or profiles for each model and are translated to the variable importance in projection (VIP), calculated as the weighted sum of squares of PLS weights (Farrés et al., 2015; Wold et al., 2001).

Temperature corrections were not applied to bring photosynthetic parameters to a standard temperature prior to model fitting absolute plot temperature was not measured at the time of image capture. As such, all leaf and plot-level models include temperature variation. No outliers were removed from predictive models presented.

Infrared Gas exchange measurements

CO₂ response

Photosynthetic (A) vs. intercellular CO₂ (C_i) response curves were collected within 30 minutes of the leaf spectral measurements on the same last fully expanded leaves to determine

$V_{c,max}$ and J_{1800} for each leaf using a portable leaf gas exchange system with leaf cuvette (*LI-6800, LICOR Biosciences, Lincoln, NE, USA*). Four machines were used by four operators to ensure unbiased sampling. Leaf temperature was determined as the mean of three measurements with a handheld IR gun (*FLIR TG54, FLIR® Systems, Inc., Wilsonville, Oregon, USA*). Leaf temperature of gas exchange was set to match this mean leaf temperature prior to each CO₂ response curve, and relative humidity set to 65%. PAR was set to 1800 $\mu\text{mol m}^{-2} \text{s}^{-1}$, and CO₂ concentrations were adjusted stepwise over a range of 50 to 2000 $\mu\text{mol mol}^{-1}$ in set increments as follows: 400, 200, 50, 100, 300, 400, 600, 900, 1200, 1500, 1800, 2000. Leaves were acclimated to chamber conditions for a minimum of 160s prior to each A/C_i curve with a minimum and maximum wait time of 160s and 200s, respectively, before each individual measurement of a response curve. $V_{c,max}$ and J_{1800} were determined from these A/C_i curves according to the mechanistic model of photosynthesis (Farquhar et al. 1980) and analyzed using a curve fitting utility developed by Sharkey et al. (2007). While light response curves were carried out prior to analysis to determine saturating light intensity as $\sim 1800 \mu\text{mol m}^{-2} \text{s}^{-1}$, we refer to maximum electron transport as J_{1800} rather than J_{max} to avoid potential false claims of true maximal capacity (Sharkey, 2016). Mesophyll conductance (g_m) was constrained according to values for tobacco at 25°C reported previously with temperature dependency incorporated from the linear relationship of g_m with temperature where $y = -0.44 + 0.058x$ (Evans and Von Caemmerer 2013).

Light response

In experiment 2, to train the P_{max} and ϕCO_2 PLSR models, photosynthetic (A) vs. irradiance (Q) response curves were collected within 30 minutes of leaf spectral measurements, on the same leaves, with a portable leaf gas exchange system (*LI-6800, LICOR Biosciences, Lincoln, NE, USA*). All environmental settings matched those for A/C_i response curves (temperature to match ambient, RH 65%), but with CO₂ set to 400 $\mu\text{mol mol}^{-1}$. Irradiance concentrations were adjusted stepwise over a range of 2000 to 0 $\mu\text{mol m}^{-2} \text{s}^{-1}$ in set increments as follows: 2000 1800, 1400, 1000, 600, 400, 200, 150, 100, 75, 50, 0.

Leaf absorption for each genotype was determined using an integrating sphere (*LI1800, LI-COR*) connected to a spectrometer (*USB-2000, Ocean Optics Inc, Dunedin, Florida, USA*) as the mean absorptance of six last fully expanded leaves (Table S1) measured on the last day of experiment 2 (July 29, 2018). A/Q curves were then corrected for absorbed irradiance (I_a). ϕCO_2

was calculated as the slope of the relationship between A and absorbed irradiance below 150 $\mu\text{mol m}^{-2} \text{s}^{-1}$. P_{max} was calculated by a non-rectangular curve fit according to Thornley and Johnson (1990) as:

$$P_{max} = \frac{\phi I_a + P_{max} - \sqrt{(\phi I_a + P_{max})^2 - 4\phi I_a \theta P_{max}}}{2\theta} - R_d$$

where P_{max} is maximum light saturated photosynthesis, ϕ is quantum yield, I_a is absorbed irradiance, θ is the curvature factor, and R_d is dark respiration rate.

Chlorophyll, Carbon and Nitrogen content

In experiment 1, immediately following each leaf spectral measurement, a 2.01cm² leaf disk was destructively harvested from each leaf using a cork borer, placed in 2 ml tubes and flash frozen in liquid nitrogen. To determine leaf chlorophyll (mg/m²) one leaf disc from each leaf was incubated in 96% (v/v) ethanol for 24 hours at 4 °C. The bleached material and ethanol were mixed (100 microliters of solution for each sample) and analyzed with a Synergy 2 photospectrometer (*BioTek Instruments, Inc, Winooski, VT, USA*) at 470 nm, 649 nm, and 665 nm (Lichtenthaler and Wellburn, 1983). To determine leaf carbon and nitrogen content (%), three more 2.01cm² leaf disks were destructively harvested, and dried until constant mass and a subset of ground tissue of known mass ($3 \pm 0.5\text{mg}$) was combusted with oxygen in an elemental analyzer (*Costech 4010; Costech Analytical Technologies*) and calibrated to %N and %C against an acetanilide standard curve.

Results

Physiological and spectral characteristics

Our models captured a wide range of natural and genetically altered trait variation over consecutive growing seasons (2017 and 2018). For performance test one, averaged plot-level measurements of observed $V_{c,max}$, J_{1800} , Chl , $Chl\ a:b$, N and C (Fig. S1A-F) include variation of

environmental and meteorological conditions (between 3 and 5 subsamples per plot), with $V_{c,max}$ from 13.4 to 359.3 $\mu\text{mol m}^{-2} \text{s}^{-1}$ (Fig. S1A), J_{1800} from 54.9 to 362.1 $\mu\text{mol m}^{-2} \text{s}^{-1}$ (Fig S1B), Chl from 0.1 to 0.3mg/m² (Fig. S1C), $Chl\ a:b$ from 1.7 to 3.7 (Fig S1D), N from 2.53 to 8.4% (Fig S1E) and C from 36.2 to 47.4% (Fig. S1F). In performance test two, from light response curves measured between July 26th and July 29th in 2018, P_{max} ranged between 4.1 and 77.7 $\mu\text{mol m}^{-2} \text{s}^{-1}$ (Fig. S1G) and ϕCO_2 ranged between 0.024 and 0.064 $\mu\text{mol m}^{-2} \text{s}^{-1}$ (Fig. S1H). Hyperspectral reflectance from all sunlit pixels per plot used to build PLSR models for all traits exhibit a peak centering at ~550 nm and high reflectivity in the NIR from 800-1300nm and a smaller peak developing from 1440-1800 nm, following the expected spectral profile pattern. However reflectance values are slightly lower than expected between 900-1250nm (Fig 3).

Plot level PLSR predictions

The corresponding reflectance spectrum from all sunlit pixels per plot (Fig. 3) paired with the observed, measured traits (Fig. S1), produced robust predictive plot level models for all traits other than ϕCO_2 . Mean spectra used for each model build in experiment 1 varied slightly, as spectra without a paired ‘ground truth’ sample for each trait were eliminated from model build datasets (Fig. 3). For example, in the SSuD genotype, J_{1800} could not be determined from gas exchange as the low Rubisco content meant this genotype was never electron transport limited but instead always Rubisco limited. Given that J_{1800} could not be calculated, the J_{1800} spectral sample size is reduced compared to the $V_{c,max}$ model build (Figs 3A and B). Similarly, a small number of leaf disk samples for leaf chlorophyll, carbon and nitrogen content were lost in transportation, storage or during analysis creating slight variation in spectral sample used for Chl (Fig. 3C) and C and N (Fig. 3D) model builds.

Using reflectance spectra from 450-900 nm only, collected with a single VNIR hyperspectral camera, $V_{c,max}$ (R^2 0.79, RMSE% 11.9), J_{1800} (R^2 0.59, RMSE% 11.5), Chl (R^2 0.87, RMSE% 10) and $Chl\ a:b$ (R^2 0.63, RMSE% 18.5), and P_{max} (R^2 0.54, RMSE% 10.6) were highly predictable from PLS hyperspectral regression models (Fig. 4, Table 2). PLSR predictions performed moderately well for C (R^2 0.47, RMSE% 18.7, Fig. 4E) and N (R^2 0.49, RMSE% 15.9%, Fig. 4F), but offered no predictability for ϕCO_2 (R^2 0.02, RMSE%, Fig. 4h) (Table 2).

When compared with the single camera models, PLSR models using both hyperspectral cameras (Fig. 5) had weakened predictive power (lower R^2 and increased RMSE%) for all traits, except *Chl a:b* (Table 2). Using both cameras, $V_{c,max}$ (R^2 0.74, RMSE% 13.1, Fig. 5B) R^2 decrease by 5% and RMSE% increased by 1.9%. However, for *Chl a:b* predictability increases when both cameras are used (R^2 0.77, RMSE% 14, Fig. 5d) where R^2 increases by 14%, and RMSE% decreases by 4.5% (Table 2).

Model loading weights indicate the importance of regions of the reflectance spectra for trait variation. For plot level PLSR predictions with a single VNIR camera (450-900nm), the region around 700 nm is important for all traits (Fig. 6). When translated to a VIP score for easier interpretation (Fig. 7), 700 nm is shown to be the most important region for $V_{c,max}$, J_{1800} and *Chl* predictions. While ~700 nm is important for all other traits, for *C* and *N*, regions from 500-650 nm, and ~820 and ~870 nm in the NIR also hold importance (Figs. 7C&D). For *Chl a:b* and P_{max} , the entire NIR from 700-900 nm holds weight. When plot level model loadings (Fig. 6) and VIP scores (Fig. 7) are compared with those from leaf level PLSR models built using the same leaves that ground truth the plot level models, they generally follow the same response pattern for all traits, with the exception of VIP scores for *Chl a:b* (Fig. 7D) and ϕCO_2 (Fig. 7H).

Leaf level PLSR models

When leaf level PLSR models were built to include different spectral ranges (500-900nm, 500-1700nm and 500-2400nm) only $V_{c,max}$, *N*, and P_{max} predictability showed minor improvement with greater spectral range (Table 3). The CV R^2 for $V_{c,max}$ remained the same when the model used reflectance from 500-1700nm, rather than 500-900nm, but there was a 2% increase when the full spectrum was used (500-2400nm). For P_{max} CV R^2 increased by 7% when spectral bandwidth matched that of both hyperspectral cameras (500-1700nm) rather than with the single VNIR only (500-900nm), but no benefit was seen with the addition of the SWIR (1700-2400nm). Leaf *N* is the only trait for which improved predictability correlated with increased spectral range, with a 3% increase in CV R^2 using 500-1700nm, and a further 7% increase using 500-2400nm (Table 2). Unlike the plot level ϕCO_2 model, ϕCO_2 was highly predictable from PLSR analysis of leaf-level spectral reflectance (CV R^2 between 0.61 and 0.63, Table 3).

For PLSR models built at the leaf level for three different spectral ranges (500-900nm, 500-1700nm, 500-2400nm, Fig 8A-H) VIP scores in the VNIR from 400-800nm were larger than those in the NIR and SWIR from 800-2400nm, for all traits other than leaf *C* and *N* contents. For *C* (Fig 8e) and *N* (Fig 8f), VIP peaks at ~1400nm and 1900nm suggest these regions also hold high importance for predictability. Comparing VIP scores for models built with a single VNIR camera (Pika II, 450-900nm) showed greater variability than those for models built with two cameras (Pika II and Pika NIR, Figs 8I-P). While all models had high VIP scores between 450-900nm, and *C* and *N* followed a similar pattern seen at the leaf level (Figs 9M-N), V_{cmax} and J_{1800} also had VIP peaks around 1100nm and 1700nm (Figs 8I-J). VIP scores for plot-level ϕCO_2 models were not shown due to the lack of predictability of this parameter with hyperspectral imaging in this study.

Discussion

Results show that photosynthetic capacity ($V_{c,max}$ and J_{1800}), maximum light saturated photosynthesis (P_{max}), and associated photosynthetic pigment contents (*C*, *N*, *Chl*, and *Chl a:b*) can be predicted using high-throughput proximal plot level hyperspectral imaging. PLSR analysis of reflectance spectra is now well established as a robust tool for estimating photosynthetic performance at the leaf level (Ainsworth et al., 2014; Serbin et al., 2012; Silva-Perez et al., 2017; Yendrek et al., 2016), and the technique holds integrity when used on plants with altered photosynthetic pathways (Meacham-Hensold et al., 2019). At a broader spatio-temporal scale, data collected with the Airbourne Visisble Infrared Imaging spectrometer (AVIRIS) has been used with PLSR analysis of reflectance spectra to successfully predict photosynthetic capacity ($V_{c,max}$) at the agroecosystem canopy level, lending lessons for ecosystem and earth system models (Serbin et al., 2015). The results here offer a tool to measure between these contrasting scales to derive photosynthetic capacity as a crop breeding selection tool. The predictive models presented in this study show the utility of hyperspectral imaging as a tool for plot-level phenotyping for superior photosynthetic performance in large scale field trials, offering potential to screen hundreds of accessions in a single day.

Spectral compositional features

Electromagnetic energy in the visible range provides the energy for photosynthesis, and absorption in the visible region specifically between 660-700 nm is of high importance for photosynthetic predictions from reflectance spectra (Fu et al., 2019; Meacham-Hensold et al., 2019; Serbin et al., 2012; Silva-Perez et al., 2017). Similarly, the region of transition from low reflectivity in the visible range to higher in the NIR (~750nm), termed ‘red-edge’, has been utilized to predict $V_{c,max}$ (Dillen et al., 2012) and is also heavily weighted in previous PLSR predictive model loadings (Meacham-Hensold et al., 2019; Silva-Perez et al., 2017; Yendrek et al., 2016). These relationships are underpinned by the importance of chlorophyll, nitrogen and Rubisco in photosynthetic processes (Evans, 1989) and the dominating influence of these pigments on reflectance spectra from 500-800nm (Curran, 1989; Elvidge, 1990; Ustin et al., 2009). Variable importance in projection (VIP) scores quantify contribution of each variable (spectral bands) to overall variance, and in this study when models were built using data from a single VNIR camera (450-900nm), the greatest peak in VIP scores are also in the chlorophyll absorption bands and the red-edge regions for $V_{c,max}$ and J_{1800} , P_{max} , Chl and N (Fig. 7) fitting with previous spectral reflectance compositional observations (Farrés et al., 2015).

Previous leaf-level studies show that some regions of the lower energy NIR, particularly ~1400 nm are also important for photosynthetic PLSR predictions (Yendrek et al., 2016). However, in this study plot level models built using reflectance in the VNIR range only (450-900nm) give greater predictability than those using reflectance from a greater spectral range (450-1700 nm) (Figs. 4 and 5, Table 3). This was unexpected and may be the result of compounding factors. In our plot-level analysis using both cameras (450-1700nm), we removed reflectance between 1313-1440nm given convolution of reflectance spectra in that region from atmospheric water absorption properties (Hill and Jones, 2000; Serbin et al., 2015), where removal of these bands is unnecessary when using a leaf clip with an artificial light source. Thus it follows, with the absence of reflectance at ~1400nm, that the spectral region detected by the single VNIR camera (400-900nm) captures the most important regions for photosynthetic predictions. This offers one possible explanation for the strength of PLSR predictions for all parameters in this study from the single VNIR camera (Fig. 4). In addition, when reflectance spectra from both cameras (450-1700nm) were used to build predictive models, VIP scores for Chl (Fig 8K), $Chl\ a:b$ (Fig 8L), and P_{max} (Fig 8P), show reflectance from the NIR above 900nm holds little to no importance (Fig 8). This is not surprising given the absorption of chlorophyll

occurs in the visible range (Ustin et al., 2009) and that P_{max} should be highly related to pigment and pigment pool distributions. However, for $V_{c,max}$ (Fig 8I), J_{1800} (Fig 8J), C (Fig 8M) and N (Fig 8N), while VIP peaks between 400-900 nm dominate, peaks at ~1150 nm and 1750 nm are present suggesting secondary importance of these regions. Despite the known spectral properties for N and C in these regions (Asner and Martin, 2008; Curran, 1989), and similarly high VIP scores around ~1100 nm in predictions of $V_{c,max}$ from airborne spectroscopy (Serbin et al., 2015), models for these three parameters built with reflectance from both cameras (450-1700 nm) rather than just the VNIR (450-900 nm) are weaker (Fig 4 and 5, Table 2).

Chl a:b is the only trait for which predictions improve when two cameras (450-1700nm) are used for the model build rather than the single VNIR (450-900nm) camera (Figs 4D and 5D). With known chlorophyll absorption dominant only in the visible range, supported by the low loading values for the leaf level *Chl a:b* models above 900nm (Fig 8D) this raises questions to the cause of improved predictability when adding reflectance spectra above 900nm. This is likely due to the dilution effect for spectral regions of physiological importance when a ratio of two physiological traits is presented. While the *Chl a:b* model is unlikely overfit given the reliance on the PRESS statistic in latent variable number selection, physiological importance is reduced allowing ‘statistical’ rather than ‘trait’ training. Thus care should be taken to eliminate spectral regions shown to hold little weight for the original trait pair when using this PLSR technique to predict ratio values.

Leaf level comparisons

In attempts to understand the relationship between spectral range and predictability power of PLSR models, we built leaf-level models for all of the plot level ground truth material measured in this study at three different spectral ranges (Table 3). For each trait, we built models first using reflectance spectra measured with the Fieldspec4 from 500-900 nm, second from 500-1700 nm, and third from 500-2400 nm. At the leaf level, with a single device measuring from 400-2500 nm and an artificial light source, the only trait prediction that improved with greater spectral range inclusion was leaf N (500-900 nm $CV R^2 = 0.66$, 500-1700 nm $CV R^2 = 0.69$, 500-2400 nm $CV R^2 = 0.76$, Table 3). The predictability of all other parameters was not increased with increased spectral range. This may be due to the almost equal importance of VIP peaks around 1400 and 1900 nm when compared with the chlorophyll and red-edge regions from

500-800 nm for nitrogen content (Fig 8F). In contrast, at the leaf level for all other predicted traits in this study, the highest VIP scores occur between 500-800 nm with only small peaks in the NIR and SWIR (Fig 8A-H) which may explain the lack of correlation between PLSR prediction power and spectral range included in the leaf level model builds for $V_{c,max}$, J_{1800} , Chl , $Chl\ a:b$, C , P_{max} and ϕCO_2 . While ϕCO_2 is not predictable with PLSR analysis at the plot level (Fig 4H and 5H), it is highly predictable at the leaf level (Table 3 and Fig S2), highlighting the need for high variation in observed trait values, to cover greater ‘trait space’ (Ely et al., 2019) for building robust models (Meacham-Hensold et al., 2019). Where observed leaf traits are averaged (between 3 and 5 subsamples) at the plot level for ϕCO_2 , observed measurement repetitions are thus reduced, shrinking the trait space and consequently model prediction strength.

Vegetative structural reflective properties and the comparative loading and VIP scores for leaf and plot-level models from 450-900 nm (Figs. 6 and 7) support the strength of plot-level models built with a single VNIR camera (Fig. 4). Loadings and VIP scores and may support a lack of improved predictability when models for the same traits are built with reflectance from two cameras that span a greater spectral range (400-1700 nm), but they do not explain the apparent reduction in predictive power (Table 3). N and C predictions in particular, should perhaps be improved when lower energy regions of the NIR are included in analysis with both cameras, due to the known absorption features properties of C and N in the NIR (Curran, 1989), and the strong VIP peaks at ~1100 nm and 1700 nm (Fig 8M-N). This unexpected reduced model strength with increased spectral range is likely due to instrumentation limitations. Hyperspectral imaging equipment for phenotyping in field trials is limited. We used two hyperspectral cameras, with different spectral resolution (Pika II: 2.1nm, Pika NIR 4.9 nm), different spatial resolution (Pika II: 7.4 μm pixel size, Pika NIR: 30 μm pixel size) and different signal to noise ratios (Pika II:198, Pika NIR: 1885), given the lack of affordability and availability of a single sensor to cover the full electromagnetic spectra. The NIR camera has greater intrinsic error.

Improving plot level hyperspectral predictions

The quality of the signal from the Pika NIR (900-1800nm) camera presents a key challenge throughout this work. Model predictions using two cameras are likely weakened due to technical limitations rather than lack of importance of particular NIR spectral regions for

physiological trait prediction. The reflectance profile from the Pika NIR imaging system ~900-1250nm is lower than expected when compared with reflectance measured with a leaf clip. Working with spectral reflectance measured by imaging systems using sunlight rather than a leaf clip with an artificial light source presents challenges with light having been influenced by the atmosphere before reaching the leaf and again after reflection before detection by a sensor. This results in a more complex signal compared with reflectance from integrated full-spectrum leaf-level devices. For example, quantification of leaf angles, removal of background noise from scattered reflectance at lower canopy levels, removal of background noise from soil (Gao et al., 2000; Verhoef, 1984) and correction for plot temperature at the time of image capture (Serbin et al., 2015) could all improve plot level model strength. Our plot level reflectance spectra is also lower between 900-1250nm than that from aircraft and other proximal hyperspectral imagers. Proximal hyperspectral imagery usually presents data captured from nadir sensors rather than pushbroom scanning platforms. At the time of our data collection, for mounting approximately a meter above target vegetation on a proximal sensing pushcart, pushbroom line sensors offered the greatest spatial resolution and affordability. However, the camera angle rotation increases directional anisotropy and coupled with light scattering from background vegetation increases our signal to noise ratio. While our automated analysis pipeline (Fig 3) very accurately accounts for radiance at time of image capture using a Teflon reference panel for accurate conversion to reflectance (Fig 2B), the signal could likely be improved with an updated nadir scanner and future incorporation of more complex radiative transfer modelling to account for background scattering. Leaf level VIP scores show less variation than plot level scores (Fig. 8) particularly in the NIR. While VIP scores are higher at the plot level, peaks do follow the same trends thus the variation is likely indicative of scattering detected by the NIR hyperspectral camera and sensor noise rather than a need to question the true importance of these regions for prediction of a given trait.

The variation in plot-level ground truthing also presents a known challenge as plot level estimations are trained with leaf-level measurements. While currently this is the only realistic ground truth method for canopy photosynthetic measurements, it is not ideal given the known limitations of applying leaf-level measurements to canopy estimations (Amthor, 1994; Baldocchi and Harley, 1995; De Pury and Farquhar, 1997; Wu et al., 2016) and the known variation in photosynthetic rates and capacities within crop canopies of the same germplasm and even within

plant crowns at the highest levels of a canopy due to variation in light environment (Niinemets, 2007). More robust plot level models could be trained with a greater number of ground truth samples, but the time taken to obtain gas exchange measurements of photosynthetic capacity is a limitation. These challenges persist for the high throughput phenotyping and the remote sensing community and as equipment develops and sensor integration capabilities advance, predictive models of the nature presented in this study will likely improve. Despite these challenges, this study proposes robust plot level predictions of key photosynthetic parameters and structural traits, that are the focus of current research efforts to increase crop yields for global food security (Evans, 2013; Ort et al., 2015).

The challenges facing agricultural production in the face of resource limitation and changing climate necessitates methods for rapid screening of large field trials for productivity and performance. The results from the automated hyperspectral image analysis pipeline we present synthesizes high resolution plot-level information to a single sunlit plot leaf reflectance spectra for use in a variety of applications. Photosynthetic predictions from PLSR analysis of this output offers a tool for rapid field phenotyping for photosynthetic performance. Such synthesis of large spatial and temporal datasets with user-friendly analysis pipelines that derive biologically relevant outcomes will be increasingly important in the fight for increased global food production. The success of predictive models with a single VNIR hyperspectral camera widens the relevance and potential application of this technique for greater utility, as reduced spectral bandwidth equates to reduced cost of acquisition and operation of hyperspectral imaging systems.

Supplementary data description

Dataset 1 – Spectrum collected with hyperspectral imaging cameras used for model builds for each trait as presented in Fig. 3. Smoothed mean, min, max, and high and low 95% confidence intervals from all spectral data are presented.

Dataset 2 – PLSR model predictions from a single VNIR hyperspectral camera (450-900nm), as shown in Fig. 4. Measured data are the average of three leaves per plot.

Dataset 3 – PLSR model predictions from two hyperspectral cameras (450-1800nm), as shown in Fig. 5. Measured data are the average of three leaves per plot.

Acknowledgments

This research was supported by Bill and Melinda Gates Foundation grant OPP1060461, titled “RIPE—Realizing increased photosynthetic efficiency for sustainable increases in crop yield” and the USDA-ARS through Project Number 5012-21000-030-00D to the Global Change and Photosynthesis Research Unit. We thank David Drag, Ben Harbaugh, Ben Thompson and Ron Edquiang for greenhouse and field plant management. Prof. Susanne von Caemmerer (*ARC Centre of Excellence for Translational Photosynthesis Research, Australian National University*) kindly provided the Rubisco Antisense *Nicotiana tabacum*. Johannes Kromdijk, Katarzyna Glowaka, Steven Driever and Stephen P. Long provided transgenic *N. tabacum* lines VPZ-23, PSBS-43, psbs-4. LMD and LCD and Paul South and Donald R. Ort provided lines Bypass AP3 and Bypass AP3/RNAi. Co-authors J.W. and S. S. were supported by the United States Department of Energy contract No. DE-SC0012704 to Brookhaven National Laboratory. We also thank Caitlin Moore, Amanda Cavanagh, Marshall Mitchell, Emily Timms, Justine Brumm, Kyle Coffland, Morgan Prinn, Alyssa Dwyer, Alex Riley, Isaac Howenstein, Jennifer Ward, Sam Jameson and Elena Pelech for assistance with the field work. Any opinions, findings, and conclusions or recommendations expressed in this publication are those of the author(s) and do not necessarily reflect the views of the U.S. Department of Agriculture. Mention of trade names or commercial products in this publication is solely for the purpose of providing specific information and does not imply recommendation or endorsement by the U.S. Department of Agriculture. USDA is an equal opportunity provider and employer.

References

- Ainsworth, E.A., Serbin, S.P., Skoneczka, J.A., Townsend, P.A.** 2014. Using leaf optical properties to detect ozone effects on foliar biochemistry. *Photosynthesis Research* 119, 65-76.
- Amthor, J.S.**, 1994. Scaling CO₂-photosynthesis relationships from the leaf to the canopy. *Photosynthesis Research* 39, 321-350.
- Asner, G.P., Martin, R.E.** 2008. Spectral and chemical analysis of tropical forests: Scaling from leaf to canopy levels. *Remote Sensing of Environment* 112, 3958-3970.
- Baldocchi, D., Harley, P.**, 1995. Scaling carbon dioxide and water vapour exchange from leaf to canopy in a deciduous forest. II. Model testing and application. *Plant, Cell & Environment* 18, 1157-1173.
- Bannon, D.**, 2009. Hyperspectral imaging: Cubes and slices. *Nature photonics* 3, 627.
- Barnes, M.L., Breshears, D.D., Law, D.J., van Leeuwen, W.J.D., Monson, R.K., Fojtik, A.C., Barron-Gafford, G.A., Moore, D.J.P.**, 2017. Beyond greenness: Detecting temporal changes in photosynthetic capacity with hyperspectral reflectance data. *PLOS ONE* 12, e0189539.
- Caemmerer, S.v., Farquhar, G.D.** 1981. Some relationships between the biochemistry of photosynthesis and the gas exchange of leaves. *Planta* 153, 376-387.
- Curran, P.J.** 1989. Remote sensing of foliar chemistry. *Remote sensing of Environment* 30, 271-278.
- Curran, P.J., Dungan, J.L., Gholz, H.L.** 1990. Exploring the relationship between reflectance red edge and chlorophyll content in slash pine. *Tree Physiol* 7, 33-48.
- De Pury, D.G.G., Farquhar, G.D.** 1997. Simple scaling of photosynthesis from leaves to canopies without the errors of big-leaf models. *Plant, Cell & Environment* 20, 537-557.
- de Wit, C.T.** 1965. *Photosynthesis of leaf canopies*. Pudoc, Wageningen, p. 57.
- Deery, D., Jimenez-Berni, J., Jones, H., Sirault, X., Furbank, R.** 2014. Proximal remote sensing buggies and potential applications for field-based phenotyping. *Agronomy* 4, 349-379.
- Demarty, J., Chevallier, F., Friend, A., Viovy, N., Piao, S., Ciais, P.** 2007. Assimilation of global MODIS leaf area index retrievals within a terrestrial biosphere model. *Geophysical research letters* 34.
- Dillen, S.Y., de Beeck, M.O., Hufkens, K., Buonanduci, M., Phillips, N.G.** 2012. Seasonal patterns of foliar reflectance in relation to photosynthetic capacity and color index in two co-occurring tree species, *Quercus rubra* and *Betula papyrifera*. *Agricultural and Forest Meteorology* 160, 60-68.
- Elvidge, C.D.** 1990. Visible and near infrared reflectance characteristics of dry plant materials. *Remote Sensing* 11, 1775-1795.
- Ely, K.S., Burnett, A.C., Lieberman-Cribbin, W., Serbin, S.P., Rogers, A.** 2019. Spectroscopy can predict key leaf traits associated with source–sink balance and carbon–nitrogen status. *Journal of Experimental Botany* 70, 1789-1799.
- Esbensen, K.H., Guyot, D., Westad, F., Houmoller, L.P.** 2002. *Multivariate data analysis: in practice: an introduction to multivariate data analysis and experimental design*. Multivariate Data Analysis.
- Evans, J., Farquhar, G.** 1991. Modelling canopy photosynthesis from the biochemistry of the C₃ chloroplast., in: Boote KJ, L.R. (Ed.), *Modelling Crop Photosynthesis: From Biochemistry to Canopy*. Crop Science Society of America, Madison, WI, pp 1–15
- Evans, J.R.** 1989. Photosynthesis and Nitrogen Relationships in Leaves of C₃ Plants. *Oecologia* 78, 9-19.

Evans, J.R. 2013. Improving Photosynthesis. *Plant Physiology* 162, 1780-1793.

Farrés, M., Platikanov, S., Tsakovski, S., Tauler, R. 2015. Comparison of the variable importance in projection (VIP) and of the selectivity ratio (SR) methods for variable selection and interpretation. *Journal of Chemometrics* 29, 528-536.

Foley, J.A., Ramankutty, N., Brauman, K.A., Cassidy, E.S., Gerber, J.S., Johnston, M., Mueller, N.D., O'Connell, C., Ray, D.K., West, P.C. 2011. Solutions for a cultivated planet. *Nature* 478, 337-342.

Fu, P., Meacham-Hensold, K., Bernacchi, C.J., Guan, K. 2019. Hyperspectral leaf reflectance as proxy for photosynthetic capacities: an ensemble approach based on multiple machine learning algorithms. *Frontiers in Plant Science* 10, 730.

Furbank, R.T., Tester, M. 2011. Phenomics--technologies to relieve the phenotyping bottleneck. *Trends Plant Sci* 16, 635-644.

Gamon, J., Penuelas, J., Field, C. 1992. A narrow-waveband spectral index that tracks diurnal changes in photosynthetic efficiency. *Remote Sensing of environment* 41, 35-44.

Gao, X., Huete, A.R., Ni, W., Miura, T. 2000. Optical-biophysical relationships of vegetation spectra without background contamination. *Remote Sensing of Environment* 74, 609-620.

Glowacka, K., Kromdijk, J., Kucera, K., Xie, J., Cavanagh, A.P., Leonelli, L., Leakey, A.D., Ort, D.R., Niyogi, K.K., Long, S.P. 2018. Photosystem II Subunit S overexpression increases the efficiency of water use in a field-grown crop. *Nature communications* 9, 868.

Glowacka, K., Kromdijk, J., Leonelli, L., Niyogi, K.K., Clemente, T.E., Long, S.P. 2016. An evaluation of new and established methods to determine T-DNA copy number and homozygosity in transgenic plants. *Plant, cell & environment* 39, 908-917.

Guan, K., Berry, J.A., Zhang, Y., Joiner, J., Guanter, L., Badgley, G., Lobell, D.B. 2016. Improving the monitoring of crop productivity using spaceborne solar-induced fluorescence. *Global change biology* 22, 716-726.

Guanter, L., Zhang, Y., Jung, M., Joiner, J., Voigt, M., Berry, J.A., Frankenberg, C., Huete, A.R., Zarco-Tejada, P., Lee, J.-E. 2014. Global and time-resolved monitoring of crop photosynthesis with chlorophyll fluorescence. *Proceedings of the National Academy of Sciences* 111, E1327-E1333.

Haboudane, D., Miller, J.R., Pattey, E., Zarco-Tejada, P.J., Strachan, I.B. 2004. Hyperspectral vegetation indices and novel algorithms for predicting green LAI of crop canopies: Modeling and validation in the context of precision agriculture. *Remote sensing of environment* 90, 337-352.

He, L., Chen, J.M., Liu, J., Zheng, T., Wang, R., Joiner, J., Chou, S., Chen, B., Liu, Y., Liu, R. 2019. Diverse photosynthetic capacity of global ecosystems mapped by satellite chlorophyll fluorescence measurements. *Remote Sensing of Environment* 232, 111344.

Hill, C., Jones, R.L. 2000. Absorption of solar radiation by water vapor in clear and cloudy skies: Implications for anomalous absorption. *Journal of Geophysical Research: Atmospheres* 105, 9421-9428.

Hudson, G.S., Evans, J.R., von Caemmerer, S., Arvidsson, Y.B., Andrews, T.J. 1992. Reduction of ribulose-1, 5-bisphosphate carboxylase/oxygenase content by antisense RNA reduces photosynthesis in transgenic tobacco plants. *Plant Physiology* 98, 294-302.

Jay, S., Bendoula, R., Hadoux, X., Féret, J.-B., Gorretta, N. 2016. A physically-based model for retrieving foliar biochemistry and leaf orientation using close-range imaging spectroscopy. *Remote sensing of environment* 177, 220-236.

Kattge, J., Knorr, W., Raddatz, T., Wirth, C. 2009. Quantifying photosynthetic capacity and its relationship to leaf nitrogen content for global-scale terrestrial biosphere models. *Global Change Biology* 15, 976-991.

Kromdijk, J., Glowacka, K., Leonelli, L., Gabilly, S.T., Iwai, M., Niyogi, K.K., Long, S.P. 2016. Improving photosynthesis and crop productivity by accelerating recovery from photoprotection. *Science* 354, 857-861.

Lawson, T., Kramer, D.M., Raines, C.A. 2012. Improving yield by exploiting mechanisms underlying natural variation of photosynthesis. *Current Opinion in Biotechnology* 23, 215-220.

Lichtenthaler, H.K., Wellburn, A.R. 1983. Determinations of total carotenoids and chlorophylls of leaf extracts in different solvents. *Biochemical Society Transactions* 11, 591-592.

Long, S.P., Bernacchi, C.J. 2003. Gas exchange measurements, what can they tell us about the underlying limitations to photosynthesis? Procedures and sources of error. *Journal of Experimental Botany* 54, 2393-2401.

Long, S.P., Zhu, X.-G., Naidu, S.L., Ort, D.R. 2006. Can improvement in photosynthesis increase crop yields? *Plant, Cell & Environment* 29, 315-330.

Meacham-Hensold, K., Montes, C.M., Wu, J., Guan, K., Fu, P., Ainsworth, E.A., Pederson, T., Moore, C.E., Brown, K.L., Raines, C. 2019. High-throughput field phenotyping using hyperspectral reflectance and partial least squares regression (PLSR) reveals genetic modifications to photosynthetic capacity. *Remote Sensing of Environment*.

Monteith, J.L., Moss, C.J. 1977. Climate and the Efficiency of Crop Production in Britain [and Discussion]. *Philosophical Transactions of the Royal Society of London. B, Biological Sciences* 281, 277-294.

Niinemets, U. 2007. Photosynthesis and resource distribution through plant canopies. *Plant, Cell & Environment* 30, 1052-1071.

Ögren, E., Evans, J.R. 1993. Photosynthetic light-response curves. *Planta* 189, 182-190.

Ort, D.R., Merchant, S.S., Alric, J., Barkan, A., Blankenship, R.E., Bock, R., Croce, R., Hanson, M.R., Hibberd, J.M., Long, S.P. 2015. Redesigning photosynthesis to sustainably meet global food and bioenergy demand. *Proceedings of the National Academy of Sciences* 112, 8529-8536.

Porcar-Castell, A., Tyystjärvi, E., Atherton, J., Van der Tol, C., Flexas, J., Pfündel, E.E., Moreno, J., Frankenberg, C., Berry, J.A. 2014. Linking chlorophyll a fluorescence to photosynthesis for remote sensing applications: mechanisms and challenges. *Journal of experimental botany* 65, 4065-4095.

Rahman, A., Sims, D., Cordova, V., El-Masri, B. 2005. Potential of MODIS EVI and surface temperature for directly estimating per-pixel ecosystem C fluxes. *Geophysical Research Letters* 32.

Ruwaimana, M., Satyanarayana, B., Otero, V., M. Muslim, A., Syafiq A, M., Ibrahim, S., Dahdouh Guebas, F. 2018. The advantages of using drones over space-borne imagery in the mapping of mangrove forests. *PLoS ONE*. 13(7) e0200288.

Savitzky, A., Golay, M.J. 1964. Smoothing and differentiation of data by simplified least squares procedures. *Analytical chemistry* 36, 1627-1639.

Serbin, S.P., Dillaway, D.N., Kruger, E.L., Townsend, P.A. 2012. Leaf optical properties reflect variation in photosynthetic metabolism and its sensitivity to temperature. *Journal of Experimental Botany* 63, 489-502.

Serbin, S.P., Singh, A., Desai, A.R., Dubois, S.G., Jablonski, A.D., Kingdon, C.C., Kruger, E.L., Townsend, P.A. 2015. Remotely estimating photosynthetic capacity, and its response to

temperature, in vegetation canopies using imaging spectroscopy. *Remote Sensing of Environment* 167, 78-87.

Serbin, S.P., Singh, A., McNeil, B.E., Kingdon, C.C., Townsend, P.A. 2014. Spectroscopic determination of leaf morphological and biochemical traits for northern temperate and boreal tree species. *Ecological Applications* 24, 1651-1669.

Sharkey, T.D. 2016. What gas exchange data can tell us about photosynthesis. *Plant, Cell & Environment* 39, 1161-1163.

Sharkey, T.D., Bernacchi, C.J., Farquhar, G.D., Singsaas, E.L. 2007. Fitting photosynthetic carbon dioxide response curves for C3 leaves. *Plant, cell & environment*. 30,1035-40.

Shi, H., Li, L., Eamus, D., Huete, A., Cleverly, J., Tian, X., Yu, Q., Wang, S., Montagnani, L., Magliulo, V. 2017. Assessing the ability of MODIS EVI to estimate terrestrial ecosystem gross primary production of multiple land cover types. *Ecological indicators* 72, 153-164.

Siegmann, B., Jarmer T. 2015 Comparison of different regression models and validation techniques for the assessment of wheat leaf area index from hyperspectral data *Int. J. Remote Sens.*, 36, 4519-4534.

Silva-Perez, V., Molero, G., Serbin, S.P., Condon, A.G., Reynolds, M.P., Furbank, R.T., Evans, J.R. 2017. Hyperspectral reflectance as a tool to measure biochemical and physiological traits in wheat. *Journal of Experimental Botany* 69, 483-496.

Smith, M.-L., Ollinger, S.V., Martin, M.E., Aber, J.D., Hallett, R.A., Goodale, C.L. 2002. Direct estimation of aboveground forest productivity through hyperspectral remote sensing of canopy nitrogen. *Ecological applications* 12, 1286-1302.

South, P.F., Cavanagh, A.P., Liu, H.W., Ort, D.R., 2019. Synthetic glycolate metabolism pathways stimulate crop growth and productivity in the field. *Science* 363, eaat9077.

Spath, H. 1985. The cluster dissection and analysis theory fortran programs examples. Prentice-Hall, Inc.

Thenkabail, P.S., Smith, R.B., De Pauw, E. 2000. Hyperspectral vegetation indices and their relationships with agricultural crop characteristics. *Remote sensing of Environment* 71, 158-182.

Thornley, J.H., Johnson, I.R. 1990. Plant and crop modelling. Clarendon Oxford.

Tilman, D., Socolow, R., Foley, J.A., Hill, J., Larson, E., Lynd, L., Pacala, S., Reilly, J., Searchinger, T., Somerville, C. 2009. Beneficial biofuels—the food, energy, and environment trilemma. *Science* 325, 270-271.

Transon J, D’andrimont R, Maignard A, Defourny P. 2018. Survey of hyperspectral earth observation applications from space in the sentinel-2 context. *Remote Sensing* 10, 157.

Ustin, S.L., Gitelson, A.A., Jacquemoud, S., Schaepman, M., Asner, G.P., Gamon, J.A., Zarco-Tejada, P. 2009. Retrieval of foliar information about plant pigment systems from high resolution spectroscopy. *Remote Sensing of Environment* 113, S67-S77.

Verhoef, W. 1984. Light scattering by leaf layers with application to canopy reflectance modeling: the SAIL model. *Remote sensing of environment* 16, 125-141.

Vogelman, T.C., Nishio, J.N., Smith, W.K. 1996. Leaves and light capture: light propagation and gradients of carbon fixation within leaves. *Trends in Plant Science* 1, 65-70.

von Caemmerer, S. 2000. *Biochemical Models of Leaf Photosynthesis*. CSIRO Publishing, Colingwood VIC 3066, Australia.

Wold, S., Sjöström, M., Eriksson, L. 2001. PLS-regression: a basic tool of chemometrics. *Chemometrics and intelligent laboratory systems* 58, 109-130.

Wu, A., Hammer, G.L., Doherty, A., von Caemmerer, S., Farquhar, G.D. 2019. Quantifying impacts of enhancing photosynthesis on crop yield. *Nature plants* 5, 380.

- Wu, A., Song, Y., van Oosterom, E.J., Hammer, G.L.** 2016. Connecting Biochemical Photosynthesis Models with Crop Models to Support Crop Improvement. *Frontiers in Plant Science* 7, 1518.
- Wylie, B.K., Johnson, D.A., Laca, E., Saliendra, N.Z., Gilmanov, T.G., Reed, B.C., Tieszen, L.L., Worstell, B.B.** 2003. Calibration of remotely sensed, coarse resolution NDVI to CO₂ fluxes in a sagebrush–steppe ecosystem. *Remote Sensing of Environment* 85, 243-255.
- Yendrek, C., Tomaz, T., Montes, C.M., Cao, Y., Morse, A.M., Brown, P.J., McIntyre, L., Leakey, A., Ainsworth, E.** 2016. High-throughput phenotyping of maize leaf physiology and biochemistry using hyperspectral reflectance. *Plant Physiology*, pp. 01447.02016.
- Yin, X., Struik, P.C.** 2017. Can increased leaf photosynthesis be converted into higher crop mass production? A simulation study for rice using the crop model GECROS. *Journal of experimental botany* 68, 2345-2360.
- Zarco-Tejada, P. J., Guillén-Climent, M. L., Hernández-Clemente, R., Catalina, A., González, M. R., & Martín, P.** 2013. Estimating leaf carotenoid content in vineyards using high resolution hyperspectral imagery acquired from an unmanned aerial vehicle (UAV). *Agricultural and Forest Meteorology*, 171-172, 281-294.
- Zarco-Tejada, P.J., Miller, J.R., Mohammed, G., Noland, T.L., Sampson, P.** 2002. Vegetation stress detection through chlorophyll a+ b estimation and fluorescence effects on hyperspectral imagery. *Journal of environmental quality* 31, 1433-1441.
- Zhang, Y., Guanter, L., Berry, J.A., Joiner, J., Tol, C., Huete, A., Gitelson, A., Voigt, M., Köhler, P.** 2014. Estimation of vegetation photosynthetic capacity from space-based measurements of chlorophyll fluorescence for terrestrial biosphere models. *Global change biology* 20, 3727-3742.
- Zhang, Y., Guanter, L., Joiner, J., Song, L., Guan, K.** 2018. Spatially-explicit monitoring of crop photosynthetic capacity through the use of space-based chlorophyll fluorescence data. *Remote sensing of environment* 210, 362-374.
- Zhu, X.-G., Long, S.P., Ort, D.R.** 2010. Improving Photosynthetic Efficiency for Greater Yield. *Annual Review of Plant Biology* 61, 235-261.

Tables

Table 1. *Nicotiana tabacum* genotypes used in this study and description of transgenic modification, with reference for detailed description of transformation.

Genotype	Year(s) grown	Transgene	Expected transgene function
Petite Havana	2017 & 2018	None (WT)	n/a
Samsun	2017 & 2018	None (WT)	n/a
Mammoth	2017	None (WT)	n/a
Single R antisense	2017	Rubisco small subunit antisense from <i>Nicotiana benthamiana</i> . 40% of WT Rubisco, background: W38 (Hudson et al., 1992)	Reduced photosynthetic capacity
Double R antisense	2017 & 2018	Rubisco small subunit antisense from <i>Nicotiana benthamiana</i> . 10% of WT Rubisco, background: W38 (Hudson et al., 1992)	Reduced photosynthetic capacity
Bypass AP3	2017 & 2018	Two transgenic genes expressing the enzyme Glycolate dehydrogenase and Malate synthase as an alternative photorespiratory pathway, background: Petite Havana (South et al., 2019)	Increased photosynthetic capacity, by reduction of energy loss associated with photorespiration.
Bypass AP3/RNAi	2018	Same as Bypass AP3 but with RNAi to down regulate native chloroplast glycolate transport, background: Petite Havana (South et al., 2019).	Increased photosynthetic capacity, by reduction of energy loss associated with photorespiration.
PSBS-43	2017& 2018	Increased PsbS mRNA levels from transformation with <i>Nicotiana benthamiana</i> Psbs coding sequence and 35S promoter, background: Petite Havana (Głowacka et al., 2018; Głowacka et al., 2016)	Increased photosynthetic capacity, due to increase in electron transport metabolite pools.
PsbS-4	2017 & 2018	Decreased PsbS mRNA levels from transformation with <i>Nicotiana benthamiana</i> Psbs coding sequence and 35S promoter, background: Petite Havana (Głowacka et al., 2018; Głowacka et al., 2016)	Reduced photosynthetic capacity, due to decreased electron transport metabolite pools.
VPZ-23	2017 & 2018	Three transgenes from <i>Arabidopsis thaliana</i> , expressing violaxanthin de-epoxidase (VDE), zeaxanthin epoxidase (ZEP) and photosystemII subunit S (psbS), background: Petite Havana (Kromdijk et al., 2016)	Increased photosynthetic capacity, due to overexpressed xanthophyll cycle enzymes.
LMD	2018	Transgene from <i>Arabidopsis thaliana</i> expressing plastid division protein (FtsZ), background: Petite Havana.	Low mesophyll density: Increased chloroplast size and decreased chloroplast number.
LCD	2018	Decreased mRNA levels of low cell density (LCD1) homologue of <i>N. tabacum</i> by RNAi, background: Petite Havana.	Low mesophyll cell density and lowered photosynthetic capacity

Table 2. PLSR stability statistics for models built with a single camera (450-900nm), and for models built with both cameras (450-1700nm).

Trait	450-900nm (Pika II)					450-1700nm (Pika II + Pika NIR)					Change in CV r ² (%)	Change in RMSE (%)
	Train r ²	CV r ²	RMSE (trait unit)	RMSE %	Bias (trait unit)	Train r ²	CV r ²	RMSE (trait unit)	RMSE %	Bias (trait unit)		
<i>V_{c,max}</i> (μmol m ⁻² s ⁻¹)	0.91	0.79	38.7	11.2	-0.49	0.96	0.74	45.3	13.1	1.64	-5%	+1.9
<i>J₁₈₀₀</i> (μmol m ⁻² s ⁻¹)	0.88	0.59	35.3	11.5	-0.39	0.95	0.52	41.1	13.4	3.42	-7%	+1.9
<i>Chl</i> (mg/m ²)	0.98	0.87	0.02	10	0.002	0.98	0.55	0.03	15	-0.0008	-32%	+5
<i>Chl a:b</i>	0.95	0.63	0.37	18.5	0.103	0.97	0.77	0.28	14	0.024	+15%	-4.5
<i>C</i> (%)	0.9	0.47	3.1	27.6	0.23	0.91	0.28	2.6	23.1	0.15	-19%	+4.4
<i>N</i> (%)	0.85	0.49	0.93	15.5	-0.032	0.95	0.40	1	17	-0.007	-9%	+1.2
<i>P_{max}</i> (μmol m ⁻² s ⁻¹)	0.82	0.54	7.77	1.06	0.12	0.91	0.50	8.52	11.6	0.75	-4%	+1
<i>φCO₂</i> (quanta/A μmol m ⁻² s ⁻¹)	0.35	0.02	3.33	8325	0.014	0.50	0.01	3.79	9475	-0.099	-0.1%	+1150

Table 3. PLSR models built at leaf-level for all traits using three different spectral ranges (500-900nm, 500-1700nm and 500-2400nm).

Spectral range (nm)	R ² Train	R ² CV	RMSECV (trait unit)	RMSE (%)	Model bias (trait unit)	Latent variable no.
<i>V_{cmax}</i> (μmol m⁻² s⁻¹)						
500-900	0.71	0.67	48.33	13.98	0.066	7
500-1700	0.75	0.67	45.21	13.08	0.497	10
500-2400	0.79	0.69	41.67	12.06	0.646	11
<i>J₁₈₀₀</i> (μmol m⁻² s⁻¹)						
500-900	0.59	0.40	38.58	13.38	1.211	11
500-1700	0.58	0.39	39.15	13.57	0.454	11
500-2400	0.53	0.40	41.38	14.35	0.017	8
<i>Chl content</i> (mg/m²)						
500-900	0.82	0.78	0.02	8.82	0.00007	10
500-1700	0.78	0.74	0.03	9.76	0.00003	6
500-2400	0.80	0.77	0.03	9.32	0.00001	6
<i>Chl a:b</i>						
500-900	0.87	0.78	0.25	8.56	-0.003	14
500-1700	0.86	0.79	0.25	8.84	0.0001	15
500-2400	0.85	0.76	0.50	7.50	0.005	13
<i>C content</i> (%)						
500-900	0.86	0.74	0.96	7.85	-0.011	15
500-1700	0.84	0.76	1.01	8.30	0.007	15
500-2400	0.86	0.75	0.95	7.84	0.016	15
<i>N content</i> (%)						
500-900	0.80	0.66	0.57	8.50	0.011	15
500-1700	0.80	0.69	0.58	8.65	0.007	15
500-2400	0.85	0.76	0.50	7.50	0.005	15
<i>P_{max}</i> (μmol m⁻² s⁻¹)						
500-900	0.63	0.50	8.04	10.92	0.12	9
500-1700	0.71	0.57	7.15	9.71	-0.04	13
500-2400	0.72	0.56	7.04	9.55	0.04	13
<i>ΦCO₂</i> (quanta/A μmol m⁻² s⁻¹)						
500-900	0.76	0.62	0.00	8.82	0.000004	11
500-1700	0.77	0.63	0.00	8.63	-0.000001	12
500-2400	0.73	0.61	0.00	9.24	0.000044	9

Figure Legends

Fig. 1, A ground-based phenotyping platform housing two hyperspectral cameras and RGB camera (A), with moveable white reflectance panel mounted at the top of canopy level (B).

Fig. 2, Example of the hyperspectral image analysis processing workflow. Images are captured in raw data mode (digital numbers) and represented as an RGB image (A). Pixels are separated into categories using K means clustering (B) to extract all sunlit leaf pixels, and converted to reflectance (C) from raw data in digital numbers (D). Mean value and standard deviation of all sunlit leaf reflectance pixels are computed (D).

Fig. 3, Mean plot level sunlit leaf reflectance for all spectrum included in plot-level PLSR models, from performance test 1, $V_{c,max}$ (A), J_{1800} (B), Chl and $Chl\ a:b$ (C), and C and N content (D) and performance test 2, P_{max} and ϕCO_2 (E). Spectrum are obtained from our automated image analysis pipeline with atmospheric water absorption band 1313-1440nm removed, and displayed with the min and max from all data and 95% confidence intervals. n = the number of plots the spectrum represent. Sample size for each trait varies dependent on the amount of viable groundtruth samples taken for each trait.

Fig. 4, Comparison between observed photosynthetic parameters and those predicted from PLS regression of plot-level sunlit leaf reflectance using a single VNIR hyperspectral camera (450-900nm) for $V_{c,max}$ (A), J_{1800} (B), Chl (C), $Chl\ a:b$ (D), C (E) and N (F) in performance test 1, and P_{max} (G) and ϕCO_2 (H) in performance test 2. Observed parameters are the mean of 3-5 leaf-level ground truth measurements and predictions are the mean of 1000 times cross-validation of the model.

Fig. 5, Comparison between observed photosynthetic parameters and those predicted from PLS regression of plot-level sunlit leaf reflectance using both VNIR hyperspectral camera (450-900nm) and NIR/SWIR (900-1700nm) cameras for $V_{c,max}$ (A), J_{1800} (B), Chl (C), $Chl\ a:b$ (D), C (E) and N (F) in performance test 1, and P_{max} (G) and ϕCO_2 (H) in performance test 2. Observed parameters are the mean of 3-5 leaf-level ground truth measurements and predictions are the mean of 1000 times cross-validation of the model.

Fig. 6, Model loadings from leaf level and plot level PLSR models from 450-900nm for all traits: $V_{c,max}$ (A), J_{1800} (B), Chl (C), $Chl\ a:b$ (D), C (E) and N (F) in performance test 1, and P_{max} (G) and ϕCO_2 (H) in performance test 2.

Fig. 7, Comparison of variable importance projection (VIP) scores from leaf level and plot level PLSR models from 450-900nm for all traits: $V_{c,max}$ (A), J_{1800} (B), Chl (C), $Chl\ a:b$ (D), C (E) and N (F) in performance test 1, and P_{max} (G) and ϕCO_2 (H) in performance test 2.

Fig. 8, PLSR model variable importance projection (VIP) scores for models built with different spectral ranges for leaf level and for $V_{c,max}$ (A), J_{1800} (B), Chl (C), $Chl\ a:b$ (D), C (E) and N (F) P_{max} (G) and ϕCO_2 (H), and at the plot level for the same traits respectively (I-P). VIP scores for plot-level ϕCO_2 models are not shown due to the lack of predictability of this parameter at the plot level.

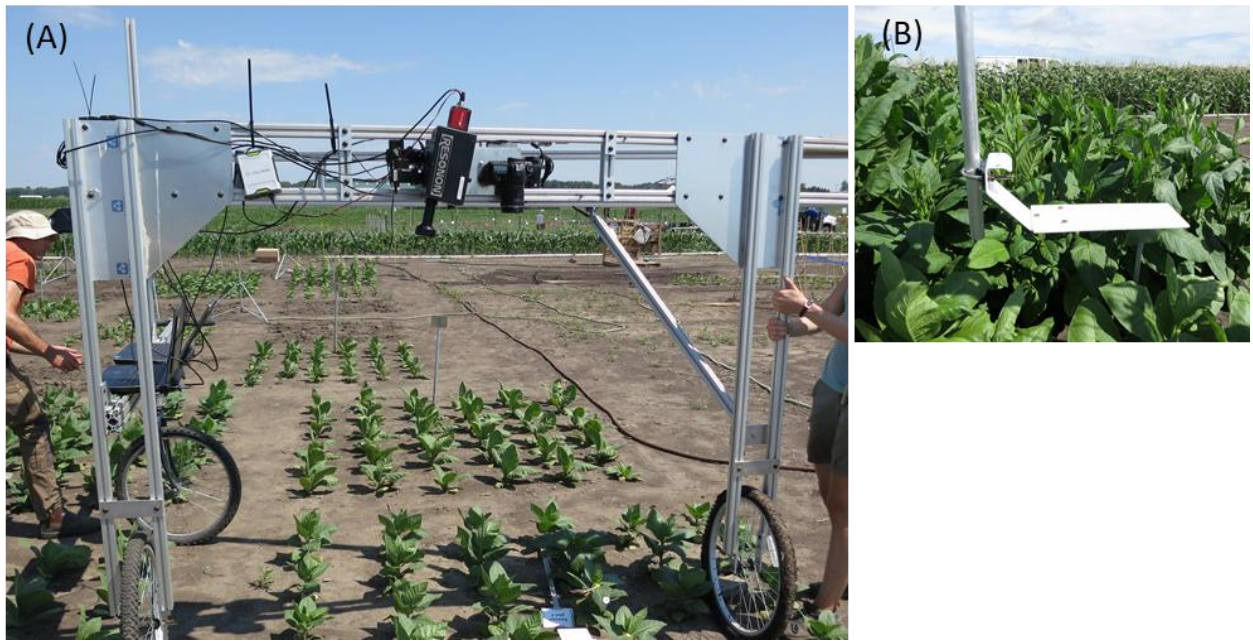


Fig 1

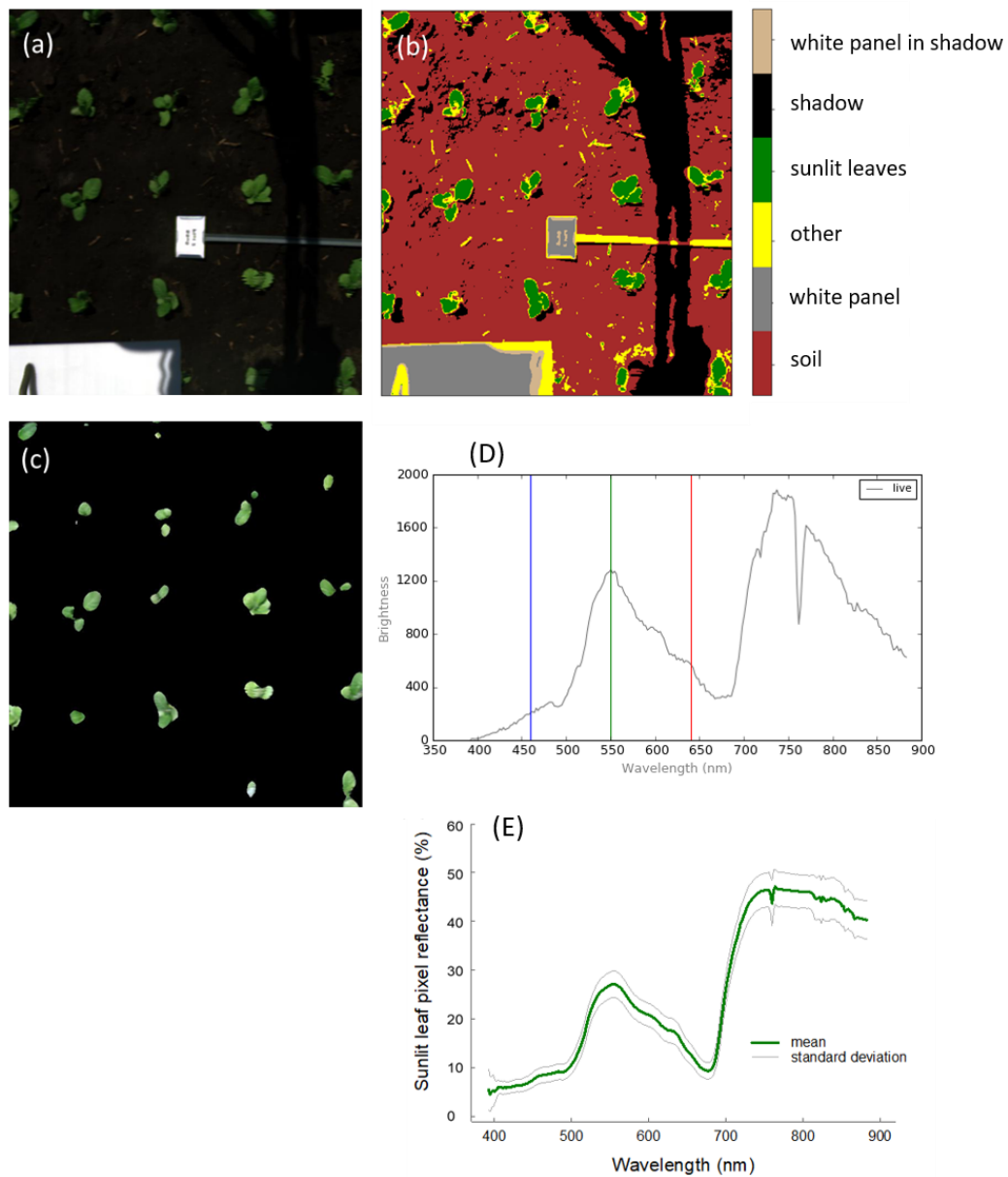


Fig 2

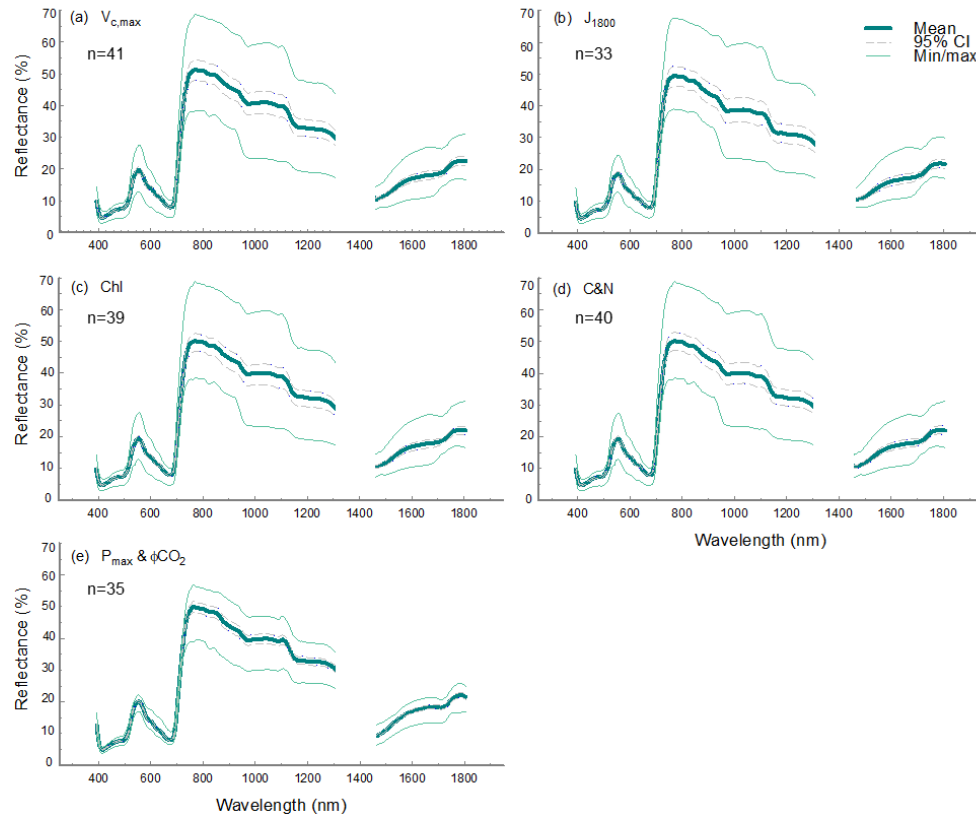


Fig 3

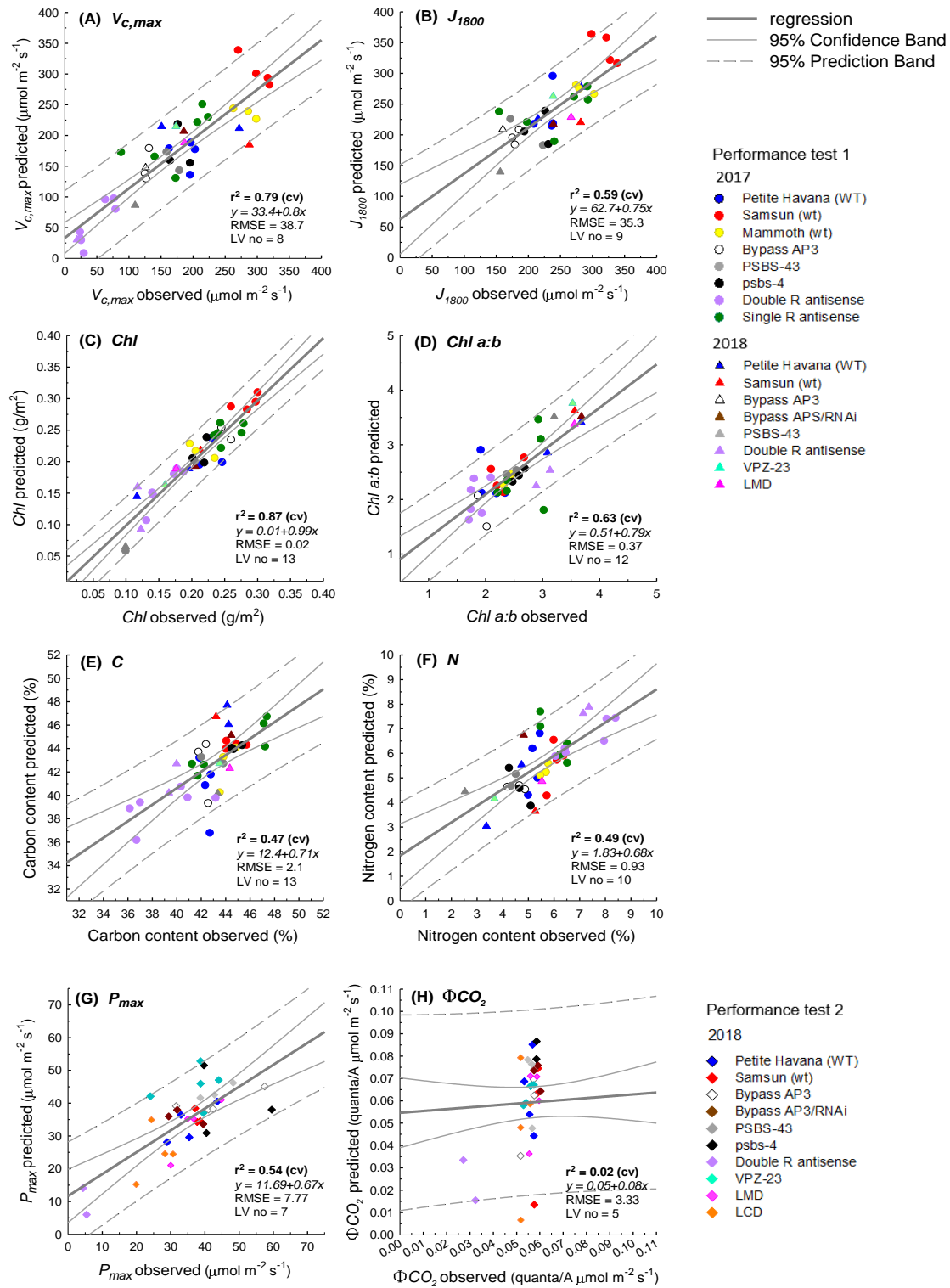


Fig 4

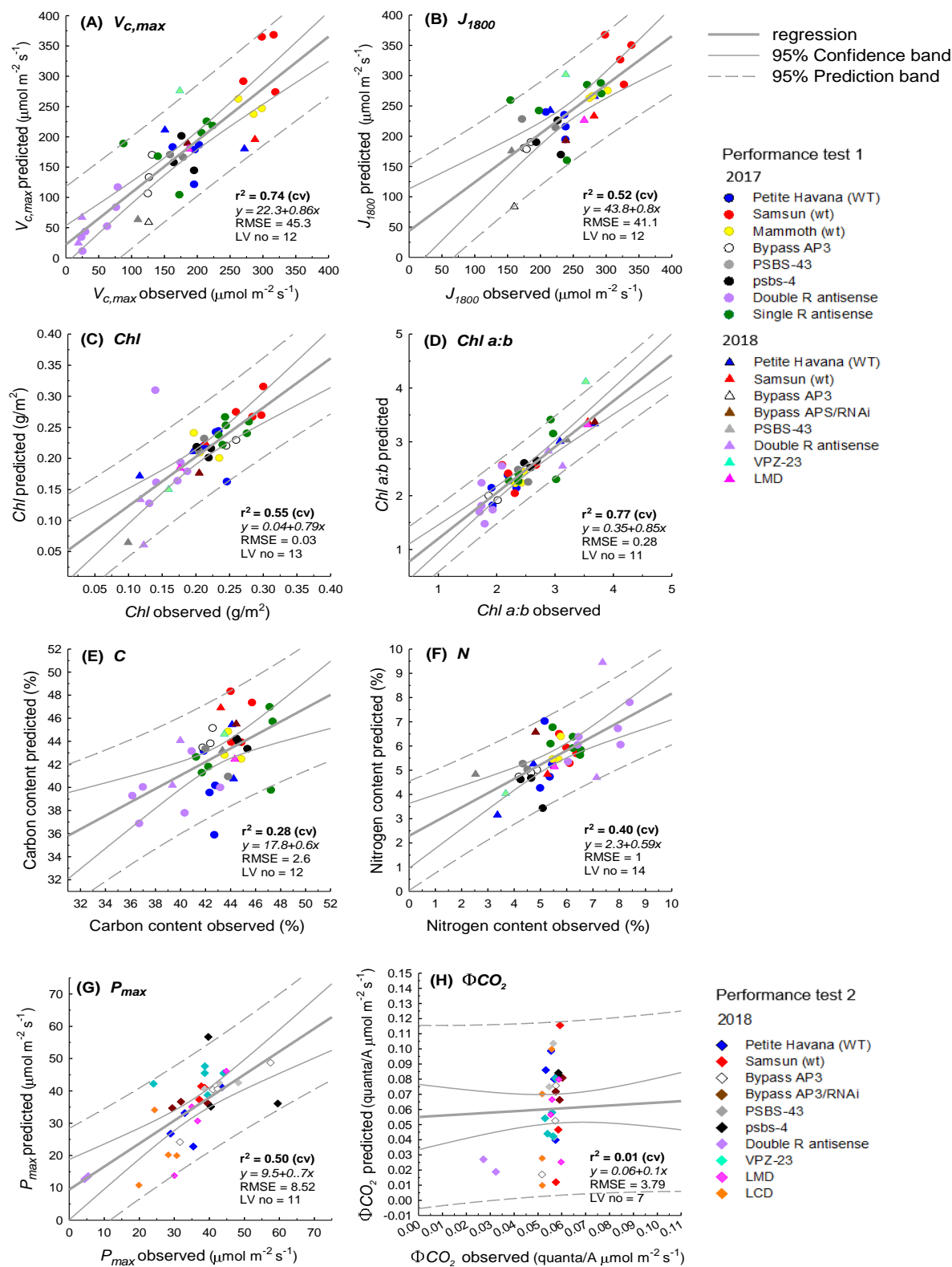


Fig 5

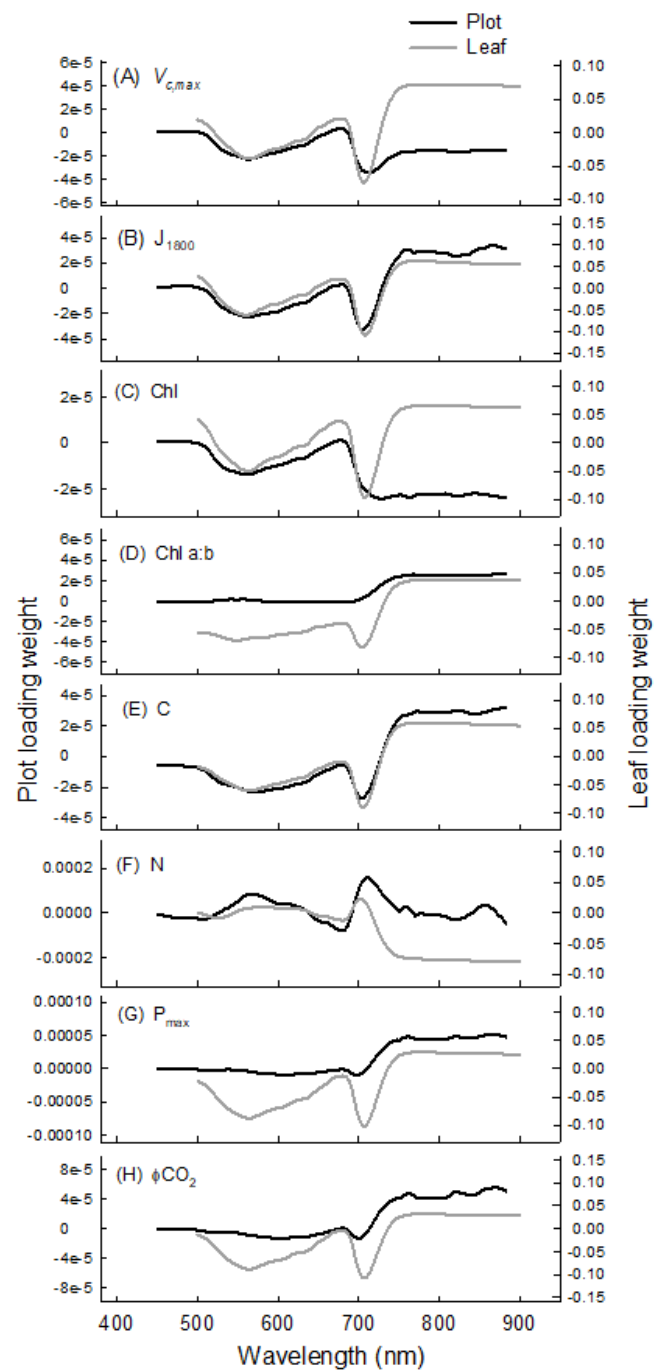


Fig 6

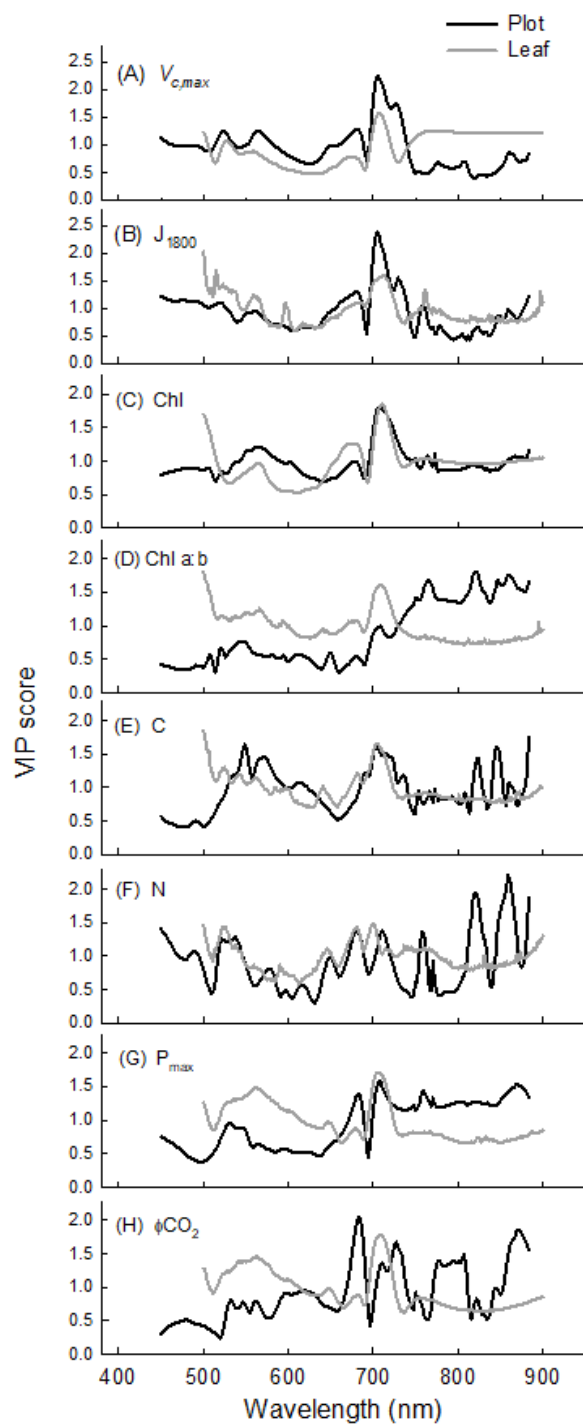


Fig 7

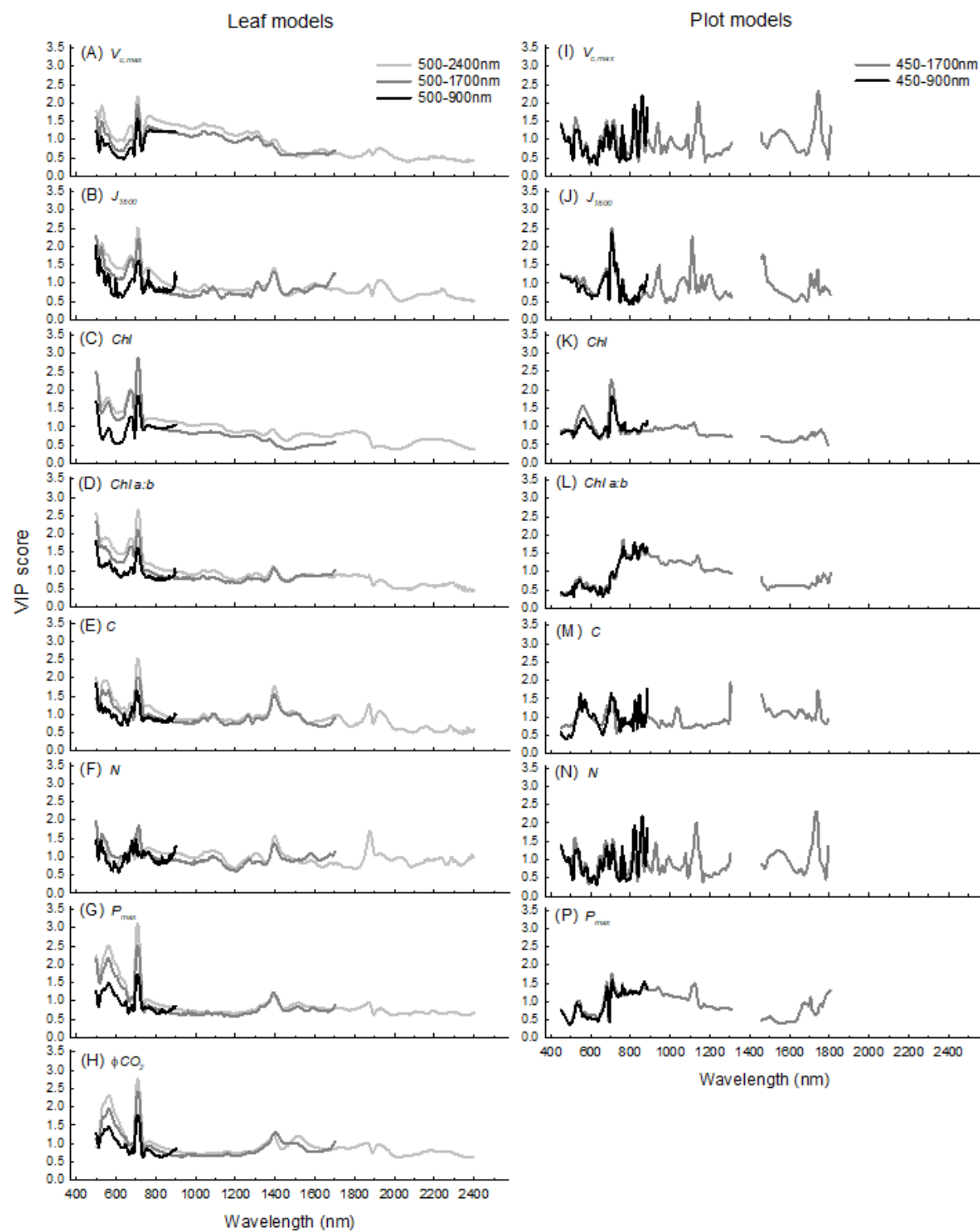


Fig 8